



Two-dimensional superstructures filled into polysulfone membranes for highly improved ultrafiltration: The case of cuprous iodide nanosheets

Jian Zhou, Dan Sun, Lei Wang, Leiming Guo, Wei Chen, Fengjiao Yu, Yong Wang*, Yang Yang*

State Key Laboratory of Materials-Oriented Chemical Engineering, College of Chemical Engineering, Nanjing Tech University, Nanjing 210009, Jiangsu, PR China



ARTICLE INFO

Keywords:

Superstructure
Polysulfone
Phase separation
Mixed-matrix membrane
Ultrafiltration

ABSTRACT

Mixed-matrix membranes blended with nanosized inorganic fillers have been widely used in ultrafiltration (UF) for large molecule separation. In this work, we provide a feasible route to construct mixed-matrix polysulfone (PSf) UF membranes *via* the nonsolvent-induced phase inversion process, utilizing sheet-like copper iodide superstructures (s-CuI) as fillers. The size of s-CuI in lateral dimension reaches micrometer scale, but the nanosheets can be well embedded in the polymer matrix with their 2D basal planes parallel to the membrane surface. On account of the stacking straight-through channel structure of s-CuI and its large dimension spanning across multiple membrane pores within the layer, the PSf membrane blended with 0.8 wt% content of s-CuI displays optimal UF performance with a pure water permeation (PWP) of 1473 L/(m² h bar) and a bovine serum albumin (BSA) rejection of 92%. In contrast, the pure PSf membrane only presents a PWP of 556 L/(m² h bar) and a BSA rejection of 58.2%. Besides, the enhancement of mechanical stability for the PSf/s-CuI 0.8% membrane is significant and the leakage of the s-CuI filler is negligible. Though the antifouling performance of the PSf/s-CuI 0.8% membrane against the protein BSA is limited, its flux is always 2–3 times higher than that of the pure PSf membrane in each step during a sequential test of fouling behavior. This study indicates that it is highly promising to employ designable superstructures as functional fillers to construct novel mixed-matrix membranes with good interfacial compatibility and superior performance.

1. Introduction

Membrane-based water treatment has distinct advantages [1–3]. In particular, ultrafiltration (UF) has important applications in various industrial fields [4,5]. Nevertheless, the performance of UF polymeric membranes, commonly made from polysulfone (PSf) [6], polyamide (PA) [7], polyethersulfone (PES) [8] and so on [9–11], is limited by the tradeoff effect between permeability and selectivity [12,13].

Mixed-matrix membrane (MMM), consisting of dispersed inorganic or organic fillers throughout the continuous polymer matrix, is the up-to-date development to overcome the limitations of polymeric membrane while minimizing changes of current manufacturing processes [14–16]. Nanoparticles are typically used as the nanosized inorganic fillers, attributable to the best surface area to volume ratio for yielding large particle/polymer interfacial areas. The high agglomerate tendency of nanoparticles in the casting solution, however, often induces the increase of the particle size, which consequently reduces the specific surface area of the nanosized fillers. More critically, the random particulate aggregates are easy to cause poor contact between the inorganic filler and the polymeric membrane chain, thus partially

damaging the final MMM structure [5,15].

Recently, it is reported that two-dimensional (2D) nanosized inorganic fillers present superiority over the zero-dimensional ones in MMMs [2,7,17]. On the one hand, the laminated structure of the 2D fillers favors their dispersion in casting solution, which then facilitates a uniform distribution of the inorganic phase in the polymeric membrane without any additives. On the other hand, the 2D fillers can spontaneously form “brick-and-mortar” architecture in the polymer matrix and effectively interfere with the molecular diffusion in the membrane separation process. In the case of porous 2D fillers, the difference in cross-plane and in-plane confinements will further lead to anisotropic molecular diffusivity and affect the permeability and selectivity of the membranes [18]. In this field, 2D nanostructures such as graphene nanoplatelets [19], clay nanosheets [20] and leaf-shaped zeolitic imidazolate framework (ZIF-L) nanoflakes [21] have been used as fillers for UF, reverse osmosis and/or pervaporation membranes, respectively. It was demonstrated that 2D fillers noticeably outperformed the near-spherical fillers in the nanocomposite membranes.

Among various fabrication methods of incorporating nanosized fillers into a polymer matrix, nonsolvent induced phase separation (NIPS)

* Corresponding authors.

E-mail addresses: yongwang@njtech.edu.cn (Y. Wang), yangy@njtech.edu.cn (Y. Yang).

<https://doi.org/10.1016/j.memsci.2019.01.042>

Received 21 March 2018; Received in revised form 7 January 2019; Accepted 27 January 2019

Available online 29 January 2019

0376-7388/ © 2019 Elsevier B.V. All rights reserved.

process has been regarded as an effective route [22]. PSf is one of the most common polymers selected to make membranes by the NIPS process due to its commercial availability, ease of processing, together with excellent mechanical, thermal, and chemical properties [6]. The NIPS method is also competent to prepare PSf membranes with an anisotropic Loeb–Sourirajan structure mostly for UF applications [16,23].

Though 2D nanomaterial is highly favored in MMMs, many inorganic materials are difficult to form 2D nanostructures due to their crystal habit. For instance, cuprous iodide (CuI) in our case, adopts a zinc blende structure without intrinsic intention to form 2D nanostructures. Nevertheless, the 2D self-assembly of tiny building blocks provides an alternative to constructing quasi-2D nanostructures in the form of either superlattice or superstructure, depending on the internal degree of order [24–26].

In this research, we successfully transform the commercial CuI powders into self-assembled 2D sheet-like CuI superstructures (s-CuI) based on the above approach. The addition of a small percentage of 2D s-CuI into PSf has significantly improved the membrane performance, by increasing both the water flux and rejection of bovine serum albumin (BSA). The lateral (in-plane) dimension of CuI nanosheets is within micrometer scale, which is normally considered unsuitable to be embedded in the ultra-thin PSf layer. However, our results verify that the s-CuI nanosheets are nicely compatible to the NIPS process, due to their preferential orientation in the hybrid membranes. Our case study provides new perspective in 2D superstructure design by assembling 0D nanoparticles. It enables recruiting more low-cost materials as functional 2D fillers in MMMs, which may broaden the application and reduce the industrial expense of MMMs.

2. Experimental

2.1. Chemicals

Polysulfone (PSf) with Mw–35000 and polyethylene glycol (PEG) with Mw–400 were obtained from Solvay and Aladdin, respectively. N, N-Dimethylacetamide (DMAc), and acetonitrile (CH₃CN, 99.8%) were purchased from Shanghai Lingfeng Chemical Reagent Company. Cuprous iodide (CuI) and polyvinylpyrrolidone (PVP, K30) were purchased from Sinooharm Chemical Reagent Co. Bovine serum albumin (BSA) was purchased from Sigma–Aldrich. All chemicals were used as received without further purification. Deionized water was used as the only component of the nonsolvent in the coagulation bath and for all the aqueous solutions.

2.2. Synthesis of CuI superstructure nanosheets

The synthesis of CuI superstructure nanosheets followed a process similar to our previous report [26]. Commercial CuI powder was first dissolved in acetonitrile by ultrasonication until transparent solution was formed with a concentration of 20 g/L (CuI–acetonitrile adducts solution). Subsequently, 30 mL of PVP aqueous solution (30 g/L) was injected into 10 mL of CuI–acetonitrile adducts solution through a syringe under vigorous magnetic stirring (800 rpm). After stirring for 1 h, the gradually formed white precipitates were collected by the removal of supernatant, followed by washing with deionized water and ethanol, and dried at room temperature.

2.3. Preparation of PSf/CuI superstructure nanosheets membranes

Asymmetric PSf/CuI superstructure nanosheets membranes were prepared by the NIPS process. For preparing the casting solution, PSf (16 wt%) and PEG (8 wt%) were first dissolved in DMAc (76 wt%) by vigorously stirring at 300 rpm for 12 h under 70 °C. Then different amounts of the prepared CuI superstructure nanosheets (0, 0.5, 0.8, and 1.0 wt% based on the overall mass of the casting solution) were added

into the polymer solution and mechanically stirred for 2 h to form a homogeneous solution. Finally, the solution was degassed under vacuum at 50 °C for 2 h.

The resultant solution was cast onto a nonwoven fabric with a casting knife to obtain a casting film. Then the supported film was coagulated in deionized water at room temperature. The solidified PSf/CuI superstructure nanosheets membranes were thoroughly washed with water to remove the residual DMAc. The prepared MMMs with different loading contents of the CuI superstructure nanosheets (0, 0.5, 0.8, and 1.0 wt% based on the casting solution) are denoted as PSf, PSf/s-CuI 0.5%, PSf/s-CuI 0.8% and PSf/s-CuI 1.0%, respectively. In addition, we annealed CuI superstructure nanosheets in air in a muffle furnace for 1 h at 280 °C and 350 °C, respectively, for partly and completely converting CuI to CuO. The resulting products were also used as fillers (0.8 wt% based on the casting solution) for preparing the MMMs according to the same method mentioned above. These two samples are denoted as PSf/s-CuI-280 0.8% and PSf/s-CuI-350 0.8%, respectively.

2.4. Structural characterizations

Surface images of the samples were recorded by a field emission scanning electron microscope (FESEM: Hitachi S4800). The membrane samples were fractured in liquid nitrogen to expose their cross sections. A thin layer of Au/Pd alloy was sputter-coated on all the membrane samples, prior to SEM observation operated at 5 kV for acquiring both the surface and cross-sectional morphologies. Transmission electron microscopes (TEM: a JEOL 1010 microscope at an accelerating voltage of 100 kV and a Hitachi HT7700 microscope at an accelerating voltage of 120 kV) were used to obtain TEM images of the CuI superstructure nanosheets and the corresponding ED pattern. The samples were dispersed in ethanol by ultrasonic treatment. The suspended particles were transferred to a carbon-coated copper grid and dried. X-ray diffraction (XRD) measurements were conducted from 10° to 80° with a scan rate of 0.2° s⁻¹ with a SmartLab diffractometer (Rigaku Corporation) equipped with a 9 kW rotating anode Cu source at 40 kV and 100 mA.

2.5. Evaluation of membrane properties and performance

The water contact angles of the membranes were surveyed on a contact angle goniometer (KRUSS DSA–100, Germany). Deionized water of 1 μL was carefully dropped on the membrane top surface. The measurement was conducted when contact equilibrium was reached between the droplet and the membrane. To minimize the experimental error, at least three different sites were tested for each sample and the average value was reported.

Pure water permeation (PWP) and the retention to BSA were measured with a stirred filtration cell (Amicon Model 8010, Millipore). The effective area of each membrane piece was 4.1 cm². The PWP (L/(m² h bar)) was calculated using the following equation:

$$\text{PWP} = \frac{V}{A \times t \times \Delta P} \quad (1)$$

where V is the volume (L) of the pure water penetrating through the membrane, A is the effective membrane area (m²), t is the operation time (h), and ΔP is the operation pressure (bar). Most of the UF experiments were carried out at 1 bar.

BSA aqueous solution with a concentration of 0.5 g/L was prepared in phosphate buffer (pH 7.3) for the retention tests. Retention rates for BSA were determined by measuring the concentrations of BSA in solution using a UV–vis spectrometer (NanoDROP 2000C, Thermo Scientific). The relative intensity of the characteristic BSA peak centered at 280 nm was tracked. The BSA rejection (R) of the UF membrane was calculated using the following equation:

$$R = \frac{C_f - C_p}{C_f} \times 100\% \quad (2)$$

where C_f is the BSA concentration in the feed, and C_p is the BSA concentration in the permeate.

Molecular weight cut off (MWCO) of the PSf/s-CuI 0.8% membrane was determined by using aqueous solutions of dextran with four different molecular weights including 10 kDa, 40 kDa, 70 kDa, and 500 kDa, which concentration was 2.5 g/L, 1.0 g/L, 1.0 g/L, and 2.0 g/L, respectively. The concentrations of the dextran solutions were analyzed by gel permeation chromatography (GPC). Based on the relation between the rejection value and the molecular weight, the MWCO value was obtained upon 90% rejection of dextran by the membrane.

Tensile strength and percentage elongation of the membranes were measured on testing strips using a microfluidic electronic universal testing machine (CMT6203, SANS, China). The strips with rectangle shape (30 mm length and 10 mm width) were cut from the supported membranes. Then the nonwoven fabrics were removed in liquid nitrogen and only the apparently homogeneous membranes were selected for the mechanical tests. At a constant loading speed of 5 mm/min with the sample holder, tensile strength applied parallel to each strip was measured, which was further converted to tensile stress according to the strip width and the strip thickness obtained from the SEM results of the membrane. The tensile stress vs. strain curves were plotted from the above data.

Thermo-gravimetric (TG) analyses were performed within the range from room temperature to 800 °C on a thermal analyzer (TA TG449F, Netzsch) at a heating rate of 10 °C/min under flowing nitrogen.

The copper concentration in the filtrate was determined by inductively coupled plasma–atomic emission spectrometry (ICP–AES) on a Jarrell–Ash 1100 instrument.

The PWP over time, the fouling resistant ability and the recycling of the PSf membrane and the PSf/s-CuI 0.8% membrane were estimated by measuring the PWP at an operation pressure of 1 bar. The PWP of

each membrane was initially measured for 2 h until a steady-state flux (J_0) was achieved. Then deionized water was substituted by BSA solution (0.5 g/L in phosphate buffer at pH 7.3) and permeate flux (J_p) was measured for 1 h. Afterwards, the membrane was thoroughly washed by deionized water under magnetic stirring for 20 min, and then the pure water was used to repeat the flux measurement (J_R) for 1 h. Finally, the antifouling property of the membranes was evaluated by flux recovery ratio (FRR) using the following equation:

$$FRR = \frac{J_R}{J_0} \times 100\% \quad (3)$$

3. Results and discussions

At room temperature CuI is a water insoluble solid. The solvent most frequently used for CuI is acetonitrile (CH_3CN) because acetonitrile can strongly solvate CuI by π backbonding, *i.e.* the electrons from the d-orbital of the Cu atom are partially transferred to the antibonding molecular orbital of acetonitrile. This electron transfer strengthens the Cu–N bond and weakens the Cu–I bond, thus leading to the formation of well-dispersed CuI–acetonitrile adducts [26]. Using acetonitrile/water as a solvent/antisolvent couple, high-yield production of CuI fine particles can be achieved by the antisolvent crystallization method. In this experiment, we first dissolved commercial CuI powder (c-CuI) in 10 mL of acetonitrile to form a transparent solution with a concentration of 20 g/L. Next, 30 mL of PVP aqueous solution (30 g/L) was injected into this solution through the syringe pinhole under vigorous magnetic stirring. A large amount of white colloidal precipitates gradually appeared with the agitating process.

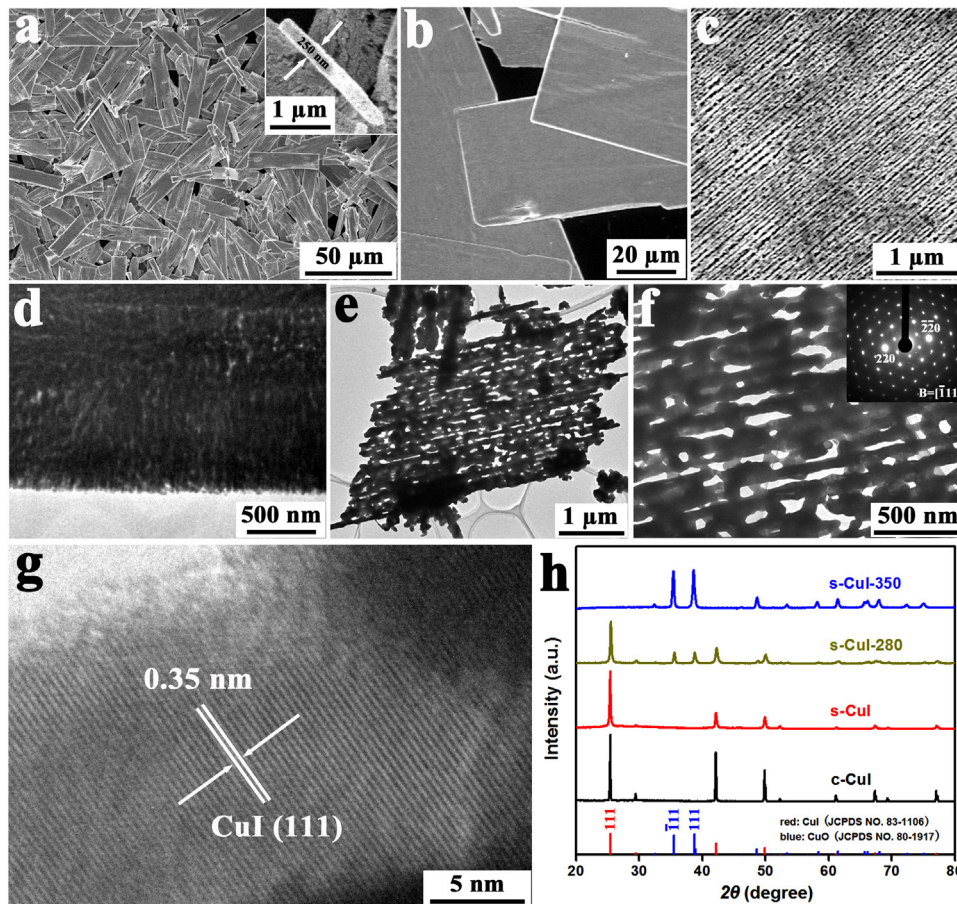


Fig. 1. SEM images of the as-prepared s-CuI: (a) general view with its inset exhibiting the thickness of a typical nanosheet; (b) close view on the edges; (c) close view on the surface. TEM images of the as-prepared s-CuI: (d) a thick nanosheet; (e) a single layer falling out from the nanosheets; (f) enlarged image of the single layer with its inset showing its corresponding ED pattern; (g) lattice resolution image of a nanoparticle constituting the single layer. (h) XRD patterns of c-CuI, s-CuI, s-CuI-280 (s-CuI subjected to annealing at 280 °C for 1 h in air) and s-CuI-350 (s-CuI subjected to annealing at 350 °C for 1 h in air).

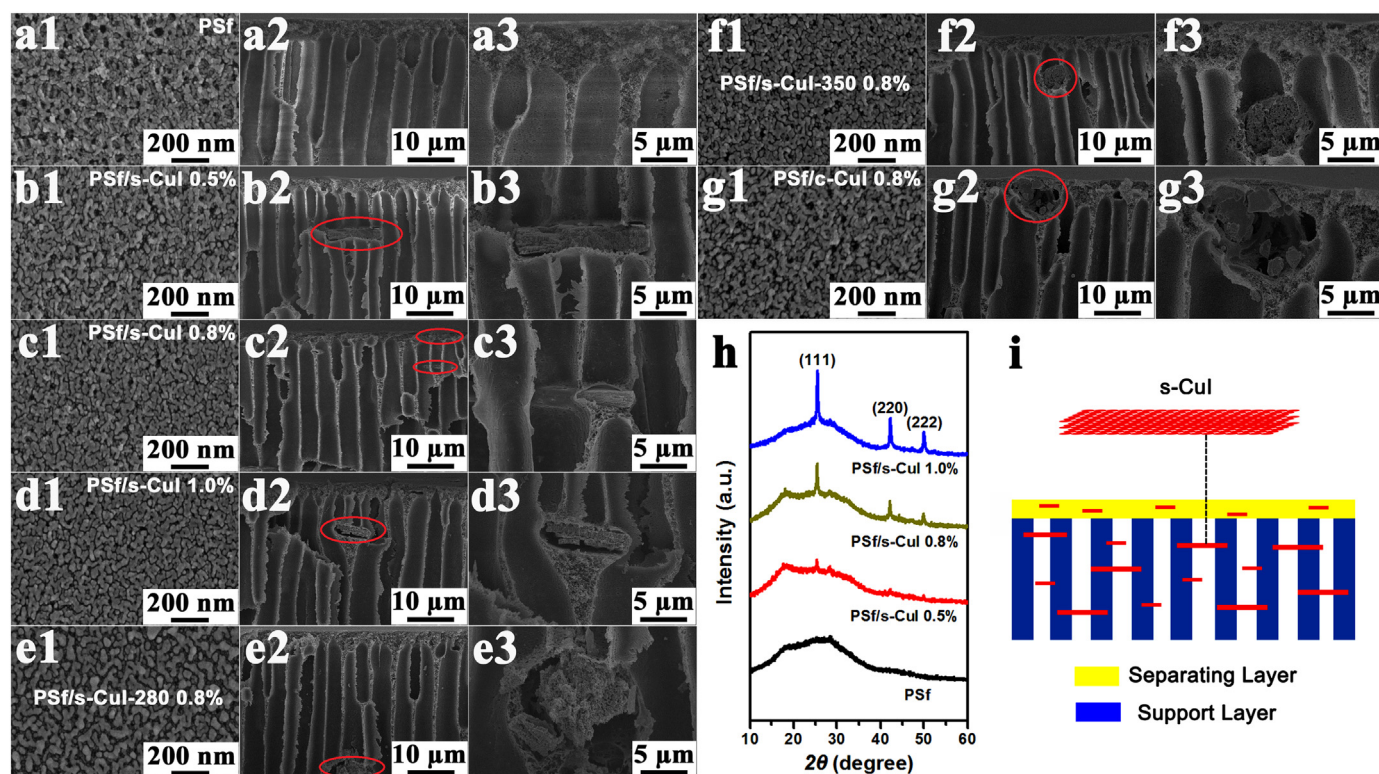


Fig. 2. Surface and cross-sectional SEM images of various membranes prepared by the NIPS process: (a) PSf; (b) PSf/s-CuI 0.5%; (c) PSf/s-CuI 0.8%; (d) PSf/s-CuI 1.0%; (e) PSf/s-CuI-280 0.8%; (f) PSf/s-CuI-350 0.8%; (g) PSf/c-CuI 0.8%. (a1–g1) are surface SEM images; (a2–g2) and (a3–g3) are cross-sectional SEM images of low and high magnifications; the red circles identify the positions of the blended fillers. (h) XRD patterns of PSf, PSf/s-CuI 0.5%, PSf/s-CuI 0.8% and PSf/s-CuI 1.0%. (i) Schematic illustration of the internal structure of the PSf-based membranes with s-CuI as the filler.

3.1. Characterization of s-CuI

Fig. 1a exhibits an SEM image of the collected precipitates, where sheet-like structures with a rectangular shape are observed. The thickness of a typical sheet shown in the inset of Fig. 1a is only 250 nm, while its width and length are within micrometer scale. The intact nanosheets have well-defined right angles and parallel sides (Fig. 1b). However, a close view reveals that the planar surface of these faceted nanosheets is not smooth and is full of hidden lines, as highlighted in Fig. 1c.

The nanosheets are analogous to fabrics woven by parallel fiber bundles. Therefore, all the obtained nanosheets are not single crystals, but superstructures arranged by small building units. It was suggested that the stabilizing effect of PVP on the initially formed CuI crystal nucleus could restrict their rapid growth through ion-by-ion attachment. In contrast, CuI superstructures with different defined geometries could be gradually developed via oriented attachment using tiny CuI crystals as building blocks [26].

We further conducted TEM investigations to study the internal structure of the nanosheets. The TEM image in Fig. 1d verifies that the nanosheet is composed of nanoparticles aligned with certain orientation. Although the image contrast indicates a large thickness of the nanosheet, a highly porous structure can be clearly observed. Especially there exist some straight-through nanosized channels penetrating the planar surface from the upper to the bottom. Fig. 1e shows a TEM image of a single layer falling out from the nanosheets, in which the fence-shaped structure conforms well to the result under SEM observation. The ED pattern corresponding to the sample area presented in Fig. 1f shows cubic symmetrical diffraction spots from the zinc-blende phase of CuI, confirming a high orientational order of the CuI nanoparticles in this 2D porous structure and the basal plane of the nanosheet is (111)-oriented. Lattice resolution image in Fig. 1g further indicates that each

highly-crystalline CuI nanoparticle is encapsulated with an amorphous thin layer of PVP. XPS analysis on s-CuI sample was carried out for more evidences. PVP is a polymer made from the N-containing monomer N-vinylpyrrolidone. XPS spectra of s-CuI sample in Fig. S1 show the presence of Cu, I and N atoms. The N 1s spectrum of s-CuI sample presents a distinguished peak centered at 399.7 eV that is assigned to the pyrrole N of PVP. Thus, the existence of PVP coating layer on the s-CuI surface is confirmed. Obviously, the average pore size in this single layer reaches a few hundred nanometers, which is much larger than the magnitude estimated from the intact CuI nanosheet (Fig. 1d). It is reasonable to suppose that the large pores were partially overlapped during the layer-by-layer stacking of the porous single layers, which significantly reduced the pore size in the resultant nanosheets [27]. In addition, the formation of CuI nanosheets is strongly dependent on the PVP concentration employed for a given amount of CuI. When the PVP concentration in the current system was doubled, the precipitated CuI superstructures in majority presented a 3D brick-like morphology and few straight-through channels were visible under TEM observations.

The XRD pattern in Fig. 1h confirms the formation of phase-pure zinc-blende CuI nanosheets (s-CuI). Because the planar surface of s-CuI is favored to place on the substrate, the intensity of diffraction originating from the (111) plane is relatively prevailing in comparison with c-CuI. When we annealed this sample at 280 °C for 1 h in air, part of the CuI was oxidized and converted to CuO (denoted as s-CuI-280), forming a mixed phase of CuI and CuO (Fig. 1h). The oriented alignment of subunits in the sheet-like structure is still maintained while the size of the interparticle pores is significantly enlarged due to the mass loss (Supporting information, Fig. S2a). When the annealing temperature was further elevated to 350 °C, the CuI was completely converted to CuO (denoted as s-CuI-350). As shown in Fig. S2b, the nanosheets initially consisting of densely-arranged building blocks are transformed

into aggregates of loosely-connected large crystals with a wide size distribution between 100 and 500 nm.

3.2. Characterization of PSf/s-CuI membranes

The surface and cross-sectional SEM images of the PSf membrane (PSf) and the membranes blended with different contents of s-CuI (PSf/s-CuI 0.5%, PSf/s-CuI 0.8%, and PSf/s-CuI 1.0%) are shown in Fig. 2a–d. For comparison, the corresponding SEM images of the hybrid membranes using the 0.8% content of s-CuI-280, s-CuI-350 and c-CuI as fillers (PSf/s-CuI-280 0.8%, PSf/s-CuI-350 0.8%, and PSf/c-CuI 0.8%) are also exhibited in Fig. 2e–g. Based on the surface view, all the blended membranes possess a certain surface roughness with an observable pore structure (Fig. 2b1–g1), similar to the pure PSf membrane (Fig. 2a1). The cross-sectional view (Fig. 2a2–g2) indicates that all the membranes present a typical asymmetric structure consisting of a top skin layer supported by a finger-like porous sub-layer. Moreover, the skin layer of each membrane shows no considerable difference in the thickness. Therefore, the entire pore structure of the PSf UF membrane is only slightly modified by the fillers via the NIPS process, which is probably due to the low additive levels in the MMMs [6,22,28].

For the membranes blended with s-CuI, the XRD patterns in Fig. 2h show gradually enhanced peak intensities of CuI with the increase of s-CuI content. Furthermore, it is revealed that the dispersion of s-CuI is nearly parallel to the membrane surface (Fig. 2b2–d2, b3–d3) even if its content reaches 20 wt% (Fig. S3). The s-CuI filler not only exists in the skin layer with parallel orientation, but spans across multiple pores in the support layer. Relative to the as-prepared s-CuI (Fig. 1a), the thickness of some nanosheets in the MMMs significantly increased, indicating the possible stacking of several nanosheets during the NIPS process. Meanwhile, we did not find any s-CuI on the membrane surface under SEM observations. However, when the annealed samples s-CuI-280 and s-CuI-350 are blended in the PSf membrane, only irregular aggregates are observed in the support layer (Fig. 2e2–f2, e3–f3), although both of them partly inherit the sheet-like morphology prior to the NIPS process. When the c-CuI is used as the filler, the large CuI crystals mostly appear underneath the membrane surface (Fig. 2g2, g3), which severely damages the skin layer by forming big voids.

Obviously, the s-CuI filler with an optimal content can be blended in the PSf membrane in a most controllable manner. The scheme of the internal structure of the PSf/s-CuI membranes is illustrated in Fig. 2i. It was reported that nonporous nanoparticles tended to migrate to the membrane surface during the phase separation process [5,14]. This conclusion is also evidenced in our experiment when using the nonporous c-CuI crystals as the filler. Relatively, the adequate dispersion of all the other fillers throughout the PSf membranes is favored by their porous structures. However, the random agglomeration of the annealed fillers s-CuI-280 and s-CuI-350 is much severer than that of the filler s-CuI. It has been elucidated that chemical modification of the fillers can greatly reduce the tendency of agglomeration during phase inversion. For instance, it is common to modify the filler surface by grafting with PVP prior to the embedding process because PVP is a typical compatilizer, which contributes to better distribution of nanoparticles [29]. For the CuI superstructure nanosheets, each building block is immobilized and segregated within a specific domain of the PVP matrix according to the formation mechanism. The existing PVP protective layer might facilitate the s-CuI to uniformly disperse in the membrane. Although annealing of the s-CuI could enhance the sintering of the subunits, the PVP was simultaneously pyrolyzed. Therefore, the annealed fillers s-CuI-280 and s-CuI-350 could not maintain the sheet-like morphology due to uncontrollable deformation and agglomeration during the NIPS process.

The wettability of PSf/s-CuI membrane surfaces was evaluated by measuring the static water contact angles. As displayed in Fig. 3, the PSf membrane shows a relatively high contact angle of 71.6°. After incorporation of the s-CuI filler with the content from 0.5 wt% to 1.0 wt

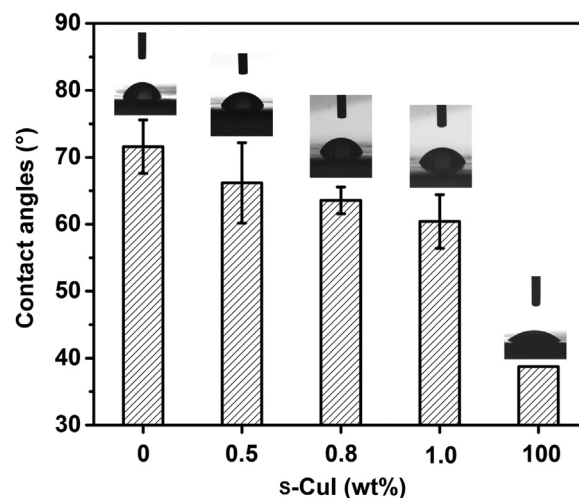


Fig. 3. The average water contact angles on the top layer of PSf/s-CuI membranes with different s-CuI loading, and on the surface of stacked sheets of s-CuI.

%, the contact angle of the MMMs gradually decreases. Nevertheless, the improvement on the hydrophilicity of the membrane surfaces is rather slight. We observe that the contact angle only decreases to 60.4° when the content of the s-CuI filler reaches 1.0 wt%. In contrast, the water contact angle on the surface of stacked sheets of s-CuI is significantly down to 38.7°, much more hydrophilic than that of the PSf membrane. Therefore, the s-CuI filler or its fragments does not directly expose on the membrane surface and impact on the surface wettability, which is in agreement with the SEM observations (Fig. 2). The increase in hydrophilicity of the PSf/s-CuI membrane surfaces mainly originates from the alteration of the inherent surface energy and pore structure of the PSf membrane subjected to the blending of the s-CuI filler [30].

3.3. Performance of PSf/s-CuI membrane

The PSf membrane has been widely exploited for UF applications because it is practical to prepare the asymmetric structure containing a separating layer and a support layer by the NIPS process. Its permeability and rejection are generally determined by the surface pore size and membrane porosity. Fig. 4 summarizes the pure water permeation

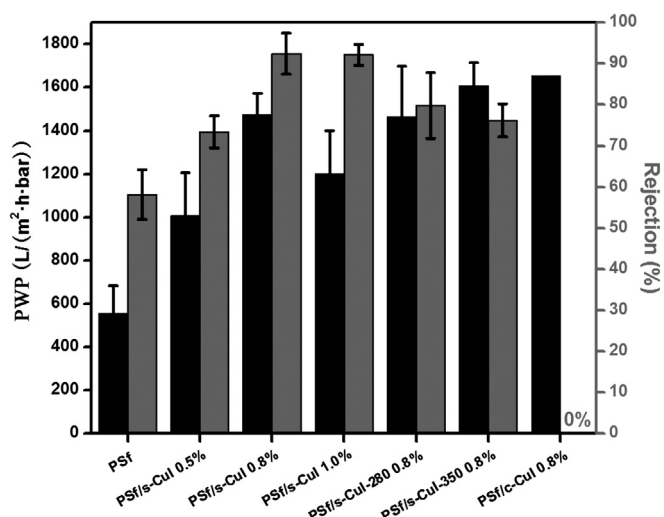


Fig. 4. Pure water permeation (PWP) and rejection (to BSA) of PSf, PSf/s-CuI 0.5%, PSf/s-CuI 0.8%, PSf/s-CuI 1.0%, PSf/s-CuI-280 0.8%, PSf/s-CuI-350 0.8% and PSf/c-CuI 0.8% membranes.

(PWP) and BSA rejection of the pure PSf membrane and the associated MMMs prepared in our experiment. The PSf membrane provides a PWP of 556 L/(m² h bar) and a retention of 58.2% to BSA in average. With the incorporation of the s-CuI filler, the PWP significantly increases and reaches a maximum of 1473 L/(m² h bar) at a loading content of 0.8 wt %, which is more than 2.6 times higher than that of the pure PSf membrane. When the loading content is further increased to 1.0 wt%, the PWP recedes to 1200 L/(m² h bar).

Overall, the trend of the PWP shows a convex profile with the increasing s-CuI content. In contrast, the increment of the BSA rejection continues until a plateau is reached. At the 0.8 wt% and 1.0 wt% loading contents, the MMMs present a comparable maximal BSA rejection up to ~92%. The above results indicate that the permeability/selectivity tradeoff relationship in the PSf membrane is overcome upon incorporation of the s-CuI filler. It is also determined that the 0.8 wt% loading content of s-CuI is optimal for enhancing both water flux and separation performance of the MMMs.

It is well accepted that the addition of hydrophilic substance in the casting solution can modify the kinetics and thermodynamics of the formation process of the polymeric membrane [27,31]. At optimal loading contents, the surface hydrophilicity of the fillers intensifies the thermodynamic immiscibility of the system and accelerates the solvent and nonsolvent exchange rate [5,32]. Hence, the surface characteristics of the fashioned membrane can be altered, and formation of a more porous structure is favored. The blending of the fillers in polymer matrix can also disrupt the polymer chain packing, thus yielding new polymer/filler interfacial areas and changing the free volume and molecular transport of the hybrid membrane [14,16]. Normally, interfacial microvoids are spontaneously formed between the two phases due to the existent defects and interfacial stresses, which lower the intrinsic resistance and improve the membrane permeability to a certain extent.

The hydrophilic s-CuI contributes to the improvement in flux, but the crucial reason is from the parallel-embedded s-CuI sheets with interior channels (Fig. 1d). Rod-like s-CuI was also blended into PSf MMMs, but we observed that the micrometer-long rods were randomly located in the membrane without preferred orientation, in which way the membrane is pierced and damaged. The stacking straight-through channels of s-CuI sheets towards the flow direction are supposed to facilitate the rapid transport of water molecules to render high water flux. Besides, the viscosity has no significant increase after s-CuI addition (before 0.65 Pa s, after 0.77 Pa s), so it is not the main reason for the rejection improvement. As highlighted in Fig. 2b3–c3, the s-CuI filler demonstrates good interfacial compatibility with the PSf matrix by forming well-aligned “brick-and-mortar” architecture. This compatible architecture enables the desirable molecular sieving effect in greatly increasing the retention to BSA. However, when the filler content is further increased to excess, for instance, 1.0 wt% in our experiment, the severer overlapping of the s-CuI filler probably occurred, which reduced the pore size in the nanosheets and generated a more tortuous pathway for water transport. As a result, the PWP of the PSf/s-CuI 1.0% membrane declines from the peak value whereas its BSA rejection maintains high.

We further investigated the impact of the annealed s-CuI fillers with the identical 0.8 wt% content on the membrane performance. As illustrated in Fig. 4, the PSf/s-CuI-280 0.8% membrane presents a PWP of 1463 L/(m² h bar), similar to that of the PSf/s-CuI 0.8% membrane, but its BSA rejection declines from 92.4% to 79.8%. The PWP of the PSf/s-CuI-350 0.8% membrane reaches a greater value of 1607 L/(m² h bar), while its BSA rejection further drops to 76.2%. Due to the removal of the PVP protective layer subsequent to annealing at elevated temperatures, the PSf/s-CuI-280 0.8% and PSf/s-CuI-350 0.8% membranes present reduced PSf/filler interfacial compatibility. The formation of unselective voids associated with interfacial defects in the separating layer enhances the water flux, but at expense of the deterioration of the BSA rejection. When c-CuI with the 0.8 wt% content is added as the filler, the obtained PSf/c-CuI 0.8% membrane is leaky, resulting in loss

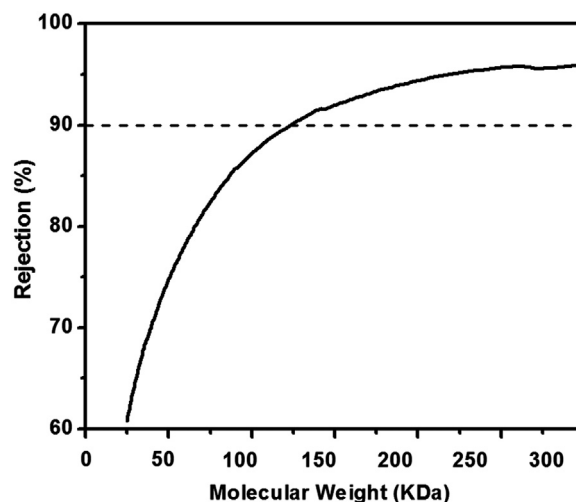


Fig. 5. Molecular weights cut-off (MWCO) curve for the PSf/s-CuI 0.8% membrane. The dashed line indicates the determination of the MWCO of the membrane.

of selectivity. Considering the separating layer of the PSf membrane is skinny, the large isodimensional c-CuI particles almost ruined the barrier and failed to function as compatible filler.

The level of BSA rejections in the range of 60–90% indicates that the MMMs blended with the s-CuI and the annealed s-CuI fillers are all in the UF range. Especially, the BSA retention of the PSf/s-CuI 0.8% membrane is maintained at 92.4% while its PWP attains 1463 L/(m² h bar), which is significantly higher than the values of MMMs prepared by filling polymer-grafted TiO₂ nanoparticles [33] and chitosan derivatives [34] in the PSf matrix (31 and 115 L/(m² h bar) on the premise of ~90% BSA retentions).

Molecular weight cut-off (MWCO) value is defined by 90% rejection of organic solutes by membranes [35], so we also tested the MWCO of the PSf/s-CuI 0.8% membrane with the superior UF performance. Its MWCO curve referring to dextran of various molecular weights is exhibited in Fig. 5, in which the MWCO (90% dextran rejection) of the MMM is determined as 122 kDa. Since the molecular weight of BSA is 67 kDa, the MMM should only offer a BSA rejection rate lower than 80%. However, the obtained retention to BSA is unexpectedly up to ~90%. In addition to the different concentrations accepted for the tests of BSA rejection and dextran MWCO, a more crucial reason might lie in the ellipsoidal shape of BSA molecules, which makes them more difficult to penetrate the membrane pores compared with glucose molecules with a linear thread-like shape [36].

Because the mechanical properties of organic–inorganic hybrid membranes usually relate to the flexibility of organic matrix and the stiffness of inorganic filler, we measured the stress–strain curves of the PSf membrane and the MMMs blended with different contents of s-CuI for evaluating the effect of the s-CuI incorporation on their mechanical stability. As shown in Fig. 6, the PSf membrane possesses a typical inferior mechanical stability with a tensile strength of 2.36 MPa and an elongation of 7.9% at break. The well-dispersed s-CuI in the PSf matrix significantly enhances the mechanical strength of the membranes at low loadings. For instance, the tensile strength and elongation at break of the PSf/s-CuI 0.5% membrane are sharply improved to 3.78 MPa and 11.5%, respectively. When the content of s-CuI increases to 0.8 wt%, the mechanical strength of the membrane is more enhanced by allowing a tensile strength of 4.43 MPa and an elongation of 12.7% at break. Further increase of the filler loading fraction to 1.0 wt% results in somewhat decreased tensile strength at break of the membrane, while its elongation attains 13.9%.

The above results indicate that the addition of the s-CuI filler could substantially boost the mechanical properties of the MMMs, where the

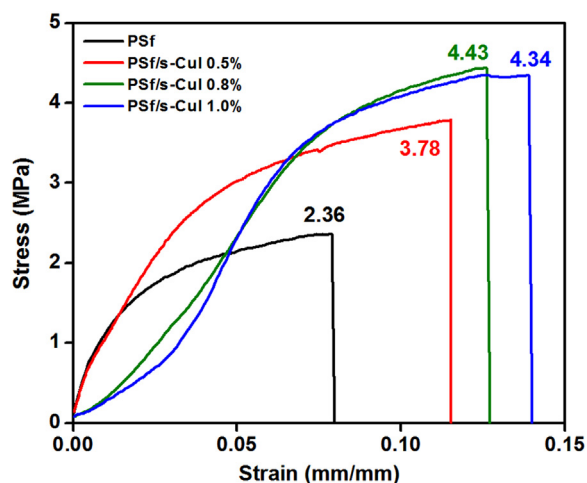


Fig. 6. Stress–strain curves for PSf, PSf/s-CuI 0.5%, PSf/s-CuI 0.8% and PSf/s-CuI 1.0% membranes.

0.8 wt% loading content is optimal, consistent with the superior ultrafiltration performance presented above (Fig. 4). We attribute such an enhancement to the formation of an intercalated structure of PSf/s-CuI, where the s-CuI with the planar construction enables the filler to be firmly confined into the membrane pores. The interfacial properties of PSf/s-CuI might be properly engineered due to the presence of the compatible PVP layer in between, which enforces the dispersed s-CuI filler as an effective cross-linking agent for the surrounding polymer chains. Consequently, the chain mobility of PSf matrix is restricted, leading to the increase of the rigidity and elasticity of the hybrid membrane [37,38]. Since more energy is needed to break down the bond between the PSf chains and the s-CuI filler, the MMMs in general display improvements of mechanical properties. The declining trend in the tensile strength with further increase in s-CuI content to 1.0 wt% probably originates from the weakened affinity between the two phases due to the severer agglomeration of the s-CuI filler. The thermal properties of PSf and PSf/s-CuI 0.8% membranes were also examined by TG analysis, as shown in Fig. S4. Both membranes exhibit similar thermal stability, but the PSf/s-CuI 0.8% membrane has more residual mass due to the incorporated s-CuI.

In a pressure-driven process such as UF, long-term operation could induce the interfacial slippage and the collapse of the membrane pores, thus incurring the risks of filler leakage from the membranes [5,15]. Hence, along with the investigation on the pure water flux of the PSf/s-CuI 0.8% membrane, we additionally examined the copper concentration in the filtrate by ICP–AES. The result shows that the copper concentration in the filtrate is only in a range of 21–40 ppb, much lower than the WHO's reference standard for copper in drinking water (1000 ppb). The insignificant amount of the filler leaching from the membrane further confirms the adequate interaction between the PSf/s-CuI constituents favored by a molecular-level synergic effect.

In view of the slightly-improved hydrophilicity of the PSf/s-CuI 0.8% membrane surface and its high BSA rejection, the antifouling performance of the MMM persists as another main concern to its ultrafiltration application [4,5,8]. Therefore, we investigated the antifouling ability of the PSf/s-CuI 0.8% membrane compared with that of the pure PSf membrane. Fig. 7 presents time-dependent flux of both the membranes during UF operation subjected to sequential fouling/washing steps. After the initial operation of deionized water for 2 h, the PWP of the PSf/s-CuI 0.8% membrane drops noticeably from 1384 L/(m² h bar) to a relatively steady flux of 936 L/(m² h bar) while the PWP of the pure PSf membrane decreases from 544 L/(m² h bar) to 328 L/(m² h bar). Such flux loss is attributable to compaction, where mechanical deformation of the solid polymer occurs under a trans-membrane pressure difference [39]. After sequential fouling/washing steps

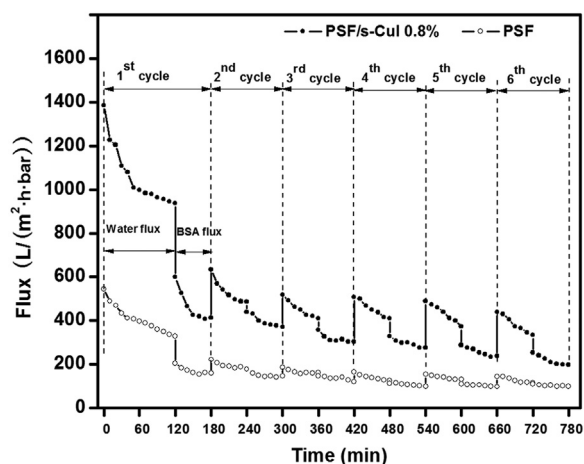


Fig. 7. Sequential test of fouling behavior for the PSf membrane and the PSf/s-CuI 0.8% membrane during filtration of BSA solution.

through BSA solution filtration, the flux recovery ratio (FRR) for the pure PSf membrane and the PSf/s-CuI 0.8% membrane are respectively 54.0% and 52.1% in the first cycle, and respectively 35.1% and 35.7% in the sixth cycle. More details of the total fouling ratio (R_t), the reversible fouling ratio (R_r) and the irreversible fouling ratio (R_{ir}) of both the membranes are given in Table S1 (Supporting Information). Notably, the PWP of the PSf/s-CuI 0.8% membrane still reaches 198 L/(m² h bar) at the end of the sixth cycle, much higher than that of pure PSf of 98 L/(m² h bar). As observed in Fig. 7, the flux reduction gradually slows down with the cyclic operation, which suggests that the fouling of BSA could be limited by its adsorption saturation in the s-CuI channels. Eventually, the PSf/s-CuI 0.8% membrane is able to keep an acceptable permeation during the sequential UF utilization, outperforming the pure PSf membrane.

The comparison of PSf/s-CuI and other PSf MMMs is summarized in Table S2. Our PSf/s-CuI shows better performance at BSA rejection and permeation. The permeability of PSf/s-CuI is particularly higher with a small concentration of CuI addition, compared to other inorganic filler MMMs such as functionalized carbon nanotubes, TiO₂ and SiO₂.

4. Conclusions

In this work, we succeeded in utilizing 2D superstructures as fillers in the mixed-matrix PSf membrane by the NIPS process. In the case study we presented, sheet-like superstructures self-assembled by CuI nanoparticles were converted directly from commercial CuI powders. We revealed that the polymer PVP first acted as an effective structure-directing agent to regulate the self-assembly of tiny CuI building blocks, then functioned as a compatibilizer to promote the dispersity of the s-CuI filler in the PSf matrix. At 0.8 wt% loading content of s-CuI, the hybrid membrane displayed optimal UF performance with a PWP of 1473 L/(m² h bar) and a BSA rejection of 92%, while the pure PSf membrane only displayed a PWP of 556 L/(m² h bar) and a BSA rejection of 58.2%. We also verified that the enhancement of mechanical stability for the PSf/s-CuI 0.8% membrane was most significant and the leakage of its s-CuI filler was negligible. This case study indicates that it is highly promising to employ designable superstructures as functional fillers to construct novel MMMs, which will broaden the application of MMMs in membrane separation processes.

Acknowledgements

This work is financially supported by grants from the National Basic Research Program of China (2015CB655301), the Key Programs of Educational Commission of Jiangsu Province (15KJA150005), a

research grant of the State Key Laboratory of Materials-Oriented Chemical Engineering (ZK201714) and the Project of Priority Academic Program Development of Jiangsu Higher Education Institutions (PAPD). Financial support from “the Youth Thousand Talents Plan” of China and “the Shuang Chuang Plan” of Jiangsu province for Y. Y. is also gratefully acknowledged.

Appendix A. Supplementary material

Supplementary data associated with this article can be found in the online version at doi:10.1016/j.memsci.2019.01.042.

References

- [1] D.L. Gin, R.D. Noble, Designing the next generation of chemical separation membranes, *Science* 332 (2011) 674–676.
- [2] G.P. Liu, Q.W. Jin, N.P. Xu, Graphene-based membranes, *Chem. Soc. Rev.* 44 (2015) 5016–5030.
- [3] M.A. Shannon, P.W. Bohn, M. Elimelech, J.G. Georgidis, B.J. Mariñas, M.A. Mayes, Science and technology for water purification in the coming decades, *Nature* 452 (2018) 301–310.
- [4] K.J. Howe, M.M. Clark, Fouling of microfiltration and ultrafiltration membranes by natural waters, *Environ. Sci. Technol.* 36 (2002) 3571–3576.
- [5] P.S. Goh, B.C. Ng, W.J. Lau, A.F. Ismail, Inorganic nanomaterials in polymeric ultrafiltration membranes for water treatment, *Sep. Purif. Rev.* 44 (2015) 216–249.
- [6] Y.N. Yang, H.X. Zhang, P. Wang, Q.Z. Zheng, J. Li, The Influence of nano-sized TiO₂ fillers on the morphologies and properties of PSF UF membrane, *J. Membr. Sci.* 288 (2007) 231–238.
- [7] A. Polotsky, V. Cherkasova, G. Polotskaya, T. Meleshko, Chemically and thermally resistant polyimide ultrafiltration membranes prepared from polyamic acid, *Desalination* 200 (2006) 341–342.
- [8] C.S. Zhao, J.M. Xue, F. Ran, S.D. Sun, Modification of polyethersulfone membranes – a review of methods, *Prog. Mater. Sci.* 58 (2013) 76–150.
- [9] L. Gemic, K. Ebert, R.H.B. Bouma, Z. Borneman, M.H.V. Mulder, H. Strathmann, Characterization of polyacrylonitrile ultrafiltration membranes, *J. Membr. Sci.* 132 (1997) 131–145.
- [10] S. Liang, Y. Kang, A. Tiraferri, E.P. Giannelis, X. Huang, M. Elimelech, Highly hydrophilic polyvinylidene fluoride (PVDF) ultrafiltration membranes via post-fabrication grafting of surface-tailored silica nanoparticles, *ACS Appl. Mater. Interfaces* 5 (2013) 6694–6703.
- [11] J. Dasgupta, S. Chakraborty, J. Sikder, R. Kumar, P. Dipankar, S. Curico, E. Drioli, The effects of thermally stable titanium silicon oxide nanoparticles on structure and performance of cellulose acetate ultrafiltration membranes, *Sep. Purif. Technol.* 133 (2014) 55–68.
- [12] M. Amit, A.L. Zydney, Permeability and selectivity analysis for ultrafiltration membranes, *J. Membr. Sci.* 249 (2005) 245–249.
- [13] G.M. Geise, D.R. Paul, B.D. Freeman, Fundamental water and salt transport properties of polymeric materials, *Prog. Mater. Sci.* 39 (2014) 1–42.
- [14] J. Yin, B.L. Deng, Polymer-matrix nanocomposite membranes for water treatment, *J. Membr. Sci.* 479 (2015) 256–275.
- [15] M.M. Pendergast, E.M.V. Hoek, A review of water treatment membrane nanotechnologies, *Environ. Sci. Technol.* 4 (2011) 1946–1971.
- [16] D. Qadir, H. Mukhtar, L.K. Keong, Mixed matrix membranes for water purification applications, *Sep. Purif. Rev.* 46 (2017) 62–80.
- [17] Y.L. Ying, Y.F. Yang, W. Ying, X.S. Peng, Two-dimensional materials for novel liquid separation membranes, *Nanotechnology* 27 (2016) 332001.
- [18] P.P. Wang, J. Ma, F.M. Shi, Y.X. Ma, Z.H. Wang, X.Y. Zhao, Behaviors and effects of differing dimensional nanomaterials in water filtration membranes through the classical phase inversion process: a review, *Ind. Eng. Chem. Res.* 52 (2013) 10355–10363.
- [19] J.G. Zhang, Z.W. Xu, W. Mai, C.Y. Min, B.M. Zhou, M.G. Shan, Y.G. Li, C.Y. Yang, Z. Wang, X.M. Qian, Improved hydrophilicity, permeability, antifouling and mechanical performance of PVDF composite ultrafiltration membranes tailored by oxidized low-dimensional carbon nanomaterials, *J. Mater. Chem.* 1 (2013) 3101–3111.
- [20] J.C. Mierzwa, V. Arieta, M. Verlage, J. Carvalho, C.D. Vecitis, Effect of clay nanoparticles on the structure and performance of polyethersulfone ultrafiltration membranes, *Desalination* 314 (2013) 147–158.
- [21] Z. Low, A. Razmjou, K. Wang, S. Gray, M. Duke, H. Wang, Effect of addition of two-dimensional ZIF-L nanoflakes on the properties of polyethersulfone ultrafiltration membrane, *J. Membr. Sci.* 460 (2014) 9–17.
- [22] G.R. Guillen, Y.J. Pan, M.H. Li, E.M.V. Hoek, Preparation and characterization of membranes formed by nonsolvent induced phase separation: a review, *Ind. Eng. Chem. Res.* 50 (2011) 3798–3817.
- [23] C.K. Mbarek, Q.T. Nguyen, O.T. Alaoui, D. Barillier, Elaboration, characterization and application of polysulfone and polyacrylic acid blends as ultrafiltration membranes for removal of some heavy metals from water, *J. Hazard. Mater.* 171 (2009) 93–101.
- [24] J.X. Gong, G.D. Li, Z.Y. Tang, Self-assembly of noble metal nanocrystals: fabrication, optical property, and application, *Nano Today* 7 (2012) 564–685.
- [25] M.P. Boneschanscher, W.H. Evers, J.J. Geuchies, T. Altantzis, B. Goris, F.T. Rabouw, S.A.P. van Rossum, H.S.J. van der Zant, L.D.A. Siebbeles, G. Van Tendeloo, I. Swart, J. Hilhorst, A.V. Petukhov, S. Bals, D. Vanmaekelbergh, Long-range orientation and atomic attachment of nanocrystals in 2D honeycomb superlattices, *Science* 344 (2014) 1377–1380.
- [26] R. Kozhummal, Y. Yang, F. Güder, U.M. Küçükbayrak, M. Zacharias, Antisolvent crystallization approach to construction of CuI superstructures with defined geometries, *ACS Nano* 7 (2013), pp. 2820–2828.
- [27] X.W. Zhang, T. Zhang, J.W. Ng, D.D. Sun, High-performance multifunctional TiO₂ nanowire ultrafiltration membrane with a hierarchical layer structure for water treatment, *Adv. Funct. Mater.* 19 (2009) 3731–3736.
- [28] J. Choi, J. Jegal, W. Kim, Fabrication and characterization of multi-walled carbon nanotubes/polymer blend membranes, *J. Membr. Sci.* 284 (2006) 406–415.
- [29] M.J. Han, S.T. Nam, Thermodynamic and rheological variation in polysulfone solution by PVP and its effect in the preparation of phase inversion membrane, *J. Membr. Sci.* 202 (2002) 56–61.
- [30] Y. Liu, X. Yue, S.L. Zhang, J.N. Ren, L.L. Yang, Q.H. Wang, G.B. Wang, Synthesis of sulfonated polyphenylsulfone as candidates for antifouling ultrafiltration membrane, *Sep. Purif. Technol.* 98 (2012) 298–370.
- [31] A. Rahimpour, S.S. Madaeni, Polyethersulfone (PES)/cellulose acetate phthalate (CAP) blend ultrafiltration membranes: preparation, morphology, performance and antifouling properties, *J. Membr. Sci.* 305 (2007) 299–312.
- [32] Q.Z. Zheng, P. Wang, Y.N. Yang, D.J. Cui, The relationship between porosity and kinetics parameter of membrane formation in PSF ultrafiltration membrane, *J. Membr. Sci.* 286 (2006) 7–11.
- [33] G. Zhang, S. Lu, L. Zhang, Q. Meng, C. Shen, J. Zhang, Novel polysulfone hybrid ultrafiltration membrane prepared with TiO₂-g-HEMA and its antifouling characteristics, *J. Membr. Sci.* 436 (2013) 163–173.
- [34] R. Kumar, A.M. Isloor, A.F. Ismail, T. Msatsura, Synthesis and characterization of novel water soluble derivative of chitosan as an additive for polysulfone ultrafiltration membrane, *J. Membr. Sci.* 440 (2013) 140–147.
- [35] A. Lee, J.W. Elam, S.B. Daring, Membrane materials for water purification: design, development, and application, *Environ. Sci.: Water Res. Technol.* 2 (2016) 17–24.
- [36] K. Hwang, P. Sz, Filtration characteristics and membrane fouling in cross-flow microfiltration of BSA/dextran binary suspension, *J. Membr. Sci.* 347 (2010) 75–84.
- [37] J.Y. Zhu, M.M. Tian, Y.T. Zhang, H.Q. Zhang, J.D. Liu, Fabrication of a novel “loose” nanofiltration membrane by facile blending with chitosan-montmorillonite nanosheets for dyes purification, *Chem. Eng. J.* 265 (2015) 184–193.
- [38] L. Yu, Y.T. Zhang, B. Zhang, J.D. Liu, H.Q. Zhang, C.H. Song, Preparation and characterization of HPEI-GO/PES ultrafiltration membrane with antifouling and antibacterial properties, *J. Membr. Sci.* 447 (2013) 452–462.
- [39] W. Chen, M.J. Wei, Y. Wang, Advanced ultrafiltration membranes by leveraging microphase separation in macrophase separation of amphiphilic polysulfone block copolymers, *J. Membr. Sci.* 525 (2017) 342–348.